Numerical experiments in separating and reattaching flows

Original
Numerical experiments in separating and reattaching flows / Cimarelli, A., Franciolini, M., Crivellini, A.. - In: PHYSICS OF FLUIDS. - ISSN 1070-6631. - 32:9(2020). [10.1063/5.0019049]

Published
DOI:10.1063/5.0019049

Numerical experiments in separating and reattaching flows

A. Cimarelli,[1, a)] M. Franciolini,[2] and A. Crivellini[3]
[1)] *DIEF, University of Modena and Reggio Emilia, 41125 Modena, Italy*
[2)] *NPP/USRA Fellow, NASA Ames Research Center, 94035 Moffet Field (CA), United States.*
[3)] *DIISM, Università Politecnica delle Marche, 60131 Ancona, Italy.*

(Dated: 3 August 2020)

We report high-order implicit Large Eddy Simulations of flows around flat plates with massive flow separation and reattachment. The aim is to provide evidence of the influence of relevant flow parameters such as the geometry of the leading-edge corner, the presence of a trailing-edge flow separation and of a flow coupling between the two sides of the plate. The results reveal that flows with right-angled corners develop taller flow recirculations which promote a very-slow instability of the bubble itself. This large-scale unsteadiness is then found to be at the basis of negative turbulence production mechanisms that in turn enhance the height of the bubble itself thus closing a self-sustained cycle. The absence of these phenomena in flows with smooth leading-edge corners is also found to explain their high sensitivity to free-stream turbulence. The observed behaviours may have strong repercussions for theories and closures of separating and reattaching flows and should be carefully taken into account in control strategies used in the applications.

I. INTRODUCTION

One of the main features of separating and reattaching flows is the combined presence of small scales due to the occurrence of turbulence and large scales due to phenomena of shedding of large-scale vortices. These phenomena nonlinearly interact themselves giving rise to a self-sustained cycle. Two main large-scale unsteadinesses are recognized: the shedding of vortices from the recirculating bubble and the low-frequency flapping mode of the recirculating region itself[1]. Despite the fact that these kinds of phenomena have been the subject of several numerical and experimental studies, their nature is still elusive and deserves further investigations[2]. Indeed, a deeper understanding of the origin of the main unsteadinesses of separating and reattaching flow may have strong repercussions on the development of control strategies relevant for a huge number of applications in natural and engineering sciences. Here, we aim at providing a further develop on the knowledge of such phenomena.

Numerical experiments have radically changed the approach to fluid dynamics. As an example, numerical simulations generally allow for broad observational capabilities that experiments cannot give. Another important feature of numerical experiments is the ability to manipulate the flow in order to remove/suppress or add/enhance physical processes and to measure the effects of those modifications on the dynamics of the flow. In this work, we make use of this ability in order to identify the main parameters controlling separating and reattaching flows and to understand the physical origin of the related mechanisms. In particular, we start by considering the flow around a rectangular cylinder with a chord-to-thickness ratio 5 (R1) which is recognized to be a very simple flow configuration for the analysis of separating and reattaching flow[3–9]. In order to appreciate the effects of shedding phenomena at the trailing edge on the behaviour of the main recirculating region, we then consider the flow around an infinite (without trailing-edge) flat plate with right-angle leading-edge corner (R2). As shown in Refs. 10–12, also this flow is recognized to be of overwhelming interest for the study of large scale recirculating flows. Regarding the case of infinite plates with leading edge separation bubble we also address the effect of the leading-edge geometry on the physics of the recirculating region by considering also an infinite flat plate with circular leading-edge corner[13,14] (R3). Finally, to address the effects of possible coupling phenomena between the shedding of large-scale vortices from the recirculating flows in the two sides of the plate, we consider a fourth type of configuration (R4). This last case reproduces the separating and reattaching flow over an infinite plate with circular leading edge such as (R3) but removing possible leading-edge interactions between the two sides of the plate by solving the flow in half domain by applying a symmetry boundary condition in the symmetry plane of the domain. Overall, the simulation of the above mentioned four types of separating and reattaching flows would allow us to identify the role played by the geometry of the leading-edge corner, by the presence or not of a trailing-edge flow separation and by the coupling phenomena between the two sides of the plate on the dynamics of the recirculating flow. A sketch of the flow configurations is reported in figure 1. Finally, the effect of free-stream turbulence will be also investigated in each flow configuration considered.

In closing this introduction, let us mention that several works have been already devoted to study the effect of relevant geometrical and flow parameters on the flow recirculation. The role played by the trailing-edge vortex shedding on the main flow processes of rectangular plates has been investigated in Ref. 6 by varying the chord-to-thickness ratio. It is found that the trailing-edge shedding has a significant influence on the self-sustained oscillations of the leading-edge shear layer. On the other hand, the role played by the shape of the leading edge on the flow recirculation dynamics has been investigated in Ref. 15 by changing the curvature of plates with rounded leading edges. It is found that changes of the leading-edge curvature deeply influence the bubble dynamic such as an increase of the bubble size, of the separation angle and of the turbulent intensity as the curvature is increased. The high sensitivity of the flow dynamics on the leading-edge geometry is further highlighted in Ref. 16 where the flow is

---

[a)] Electronic mail: andrea.cimarelli@unimore.it

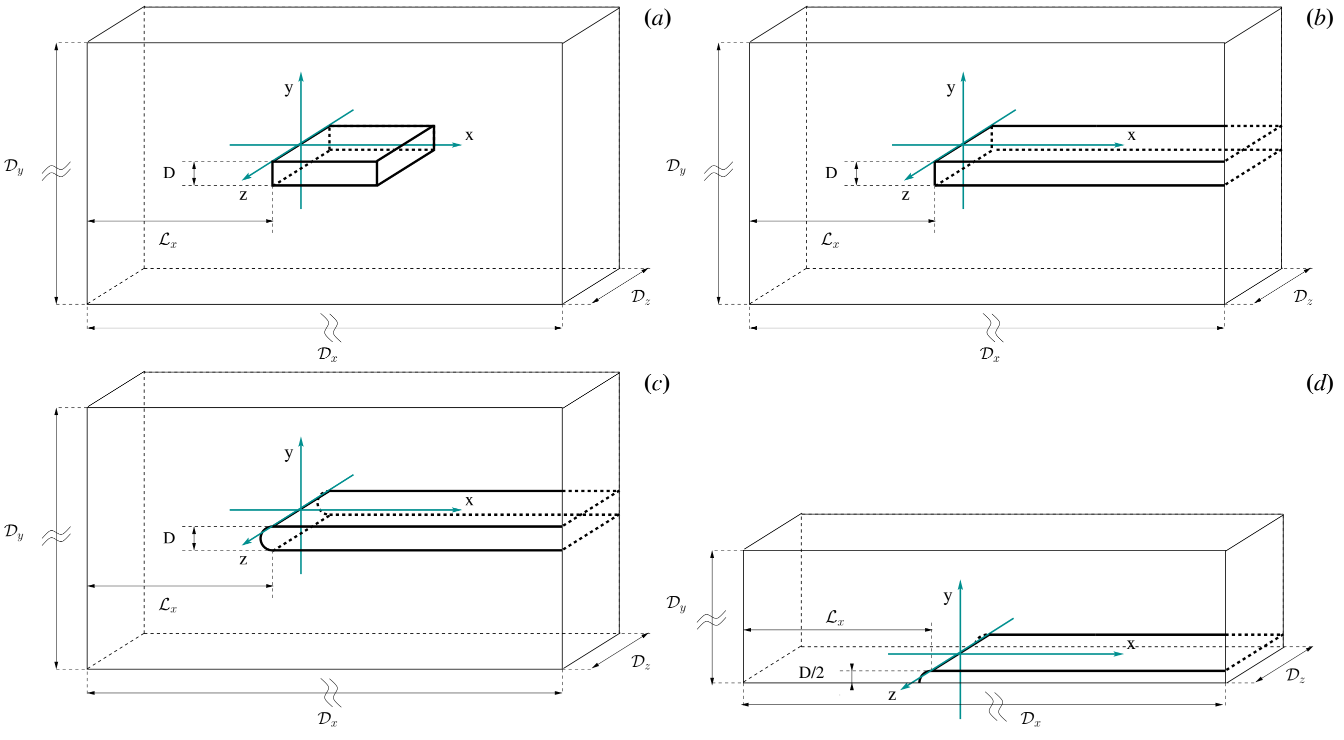

FIG. 1. Flow configurations. (a) Flow around a rectangular cylinder, R1. (b) Flow over an infinite flat plate with right-angle corner, R2. (c) Flow over an infinite flat plate with circular leading edge, R3. (d) Flow over half the domain of a flat plate with circular leading edge, R4.

found to be modified also by the introduction of very small roundings of the leading-edge corners of the order of manufacturing tolerances in experiments. Also the role played by the free-stream turbulence on the main processes of separating and reattaching flows has been investigated in several works, here we mention only few of them e.g. Refs. 17–21. The overall effect of free-stream turbulence is found to produce a more rapid transition in the leading-edge shear leading to a reduction of the reattachment length. Similar effects are reported by increasing the Reynolds number, see e.g. Refs. 2 and 22. Contrary to the mentioned works, here we address simultaneously the effects of different parameters such as the leading-edge geometry, the presence of a trailing-edge separation and the free-stream turbulence. The main goal is to give a general description of the physics of the flow recirculation that is able to explain the effects of all the geometrical and flow parameters considered.

The paper is organized as follows. In section §II the details and parameters of the numerical simulations are reported. The results of the different flow configurations are analysed in terms of instantaneous flow topology in section §III, while in sections §IV and §V the mean flow statistics are reported. The energetics of the different flow configurations are addressed in section §VI by means of a study of the turbulence production mechanisms. Finally, the effect of free-stream turbulence on the different flow configurations is analysed in section §VII. The paper is closed by final remarks in section §VIII.

II. NUMERICAL PROCEDURE AND SIMULATIONS

To handle the incompressible Navier-Stokes equations, we use an unstructured high-order Discontinuous Galerkin (DG) solver. The numerical fluxes solving the discontinuous approximation of the solution at the interface between elements have been properly defined following the technique proposed in Refs. 23–25. On the other hand, the second form of the Bassi and Rebay scheme[26] has been used for the viscous terms. The resulting discretization is fully coupled and time consistent. Time integration is performed through the four stage, order three linearly implicit Rosenbrok scheme[27]. Implicit schemes usually require the evaluation of the Jacobian matrix, which can be, particularly for a high-order method, an expensive task. To speed-up the solution process the DG solver uses a matrix-free flexible GMRES linear solver preconditioned by p-multigrid algorithm requiring, at the highest order, the evaluation of only the diagonal blocks of the Jacobian matrix. For more details the readers are referred to Ref. 28. The advantage of high order DG discretizations is given by the fact that it is possible to achieve the same spatial resolution with a reduced number of degrees of freedom (DOFs) than standard methods[29–31].

Another important advantage of the DG discretization is that the method shows numerical properties that are particularly suitable for the solution of turbulent flows with implicit Large Eddy Simulation (ILES) approaches[32]. In fact, the dissipation of the numerical scheme behaves like a spectral cut-off filter, which mimics the role of subgrid-scale mod-

Case	Re	$\mathscr{L}_x$	$\mathscr{D}_x \times \mathscr{D}_y \times \mathscr{D}_z$	N_e	(DoF)	Δy	Δz	Δt
R1	3000	72	$200 \times 151 \times 5$	52695	$4.4 \cdot 10^6$	0.0042	0.076	0.025
R2	3000	20	$36 \times 50 \times 5$	29538	$2.5 \cdot 10^6$	0.0039	0.127	0.05
R3	3450	12	$28 \times 17 \times 2$	38320	$3.2 \cdot 10^6$	0.0023	0.045	0.05
R4	3450	12	$28 \times 8.5 \times 2$	18820	$1.6 \cdot 10^6$	0.0023	0.045	0.05

TABLE I. Parameters of the simulations. Re is the Reynolds number defined as $Re = U_\infty D/\nu$. $\mathscr{L}_x$ is the distance from the inlet of the plate and $\mathscr{D}_x \times \mathscr{D}_y \times \mathscr{D}_z$ are the domain dimensions. N_e is the number of elements of the computational grid while DoF are the degrees of freedom of the corresponding solutions obtained using a sixth order polynomial scheme. Δy and Δz are the wall-normal and spanwise resolutions evaluated as the height and width of the first cell near the wall divided by the directional number of DoF. Finally, Δt is the temporal resolution.

els. ILES simulations of canonical flow problems preformed with the present code can be found in Ref. 33. A relevant benefit of the DG-ILES approach is given by the fact that the method does not introduce any unphysical subgrid dissipation in the regions of the flow where the field is fully resolved such as in the laminar flow regions. This property is particularly important in transitional flows, such as the ones investigated in the present work where laminar, transitional and turbulent free-shear regions are simultaneously present.

In this work all the computations are performed adopting a sixth order polynomial representation of the solution, for both the velocity components and pressure, which means that the velocities are 7^{th} order accurate while pressure is 6^{th} order accurate. A structured Cartesian mesh made of hexahedra is used in the near plate region. This near plate hexahedral mesh is uniform in the z direction and stretched in the x and y directions in order to ensure a sufficient resolution in the near-wall, shedding and reattachment regions. The height and width of the near-wall elements is reported in table I. On the other hand, outside this near plate region, an unstructured grid is used which is strongly coarsened moving away from the plate to save computational resources. Further details on the mesh properties can be found in Ref. 28. The resulting number of grid elements is reported in table I where other parameters of the simulations such as domain lengths, degrees of freedom, spatial and temporal resolutions are reported. For all the flow cases, in accordance to the standard approach for a DG discretization, weak imposition of boundary conditions are employed. In other words boundary condition data together with extrapolated values define an external state and numerical fluxes are used, as for the internal faces, for solving the discontinuous solution at the boundaries faces. An unperturbed free-stream velocity U_∞ is applied at the inlet and a pressure condition is used at the outlet. On the other hand, in the top and bottom boundaries a weak imposition of the free-stream condition is used for the flow cases R1 and R2 while a symmetry condition is applied for R3 and R4. Finally a periodic boundary condition is applied in the spanwise direction. The domain, boundary condition and Reynolds number differences between the flow configurations R1 and R2 with respect to R3 and R4 are given by the need of replicate benchmark data of the corresponding flow cases present in literature, e.g. Refs. 8, 9, 12–14. The solutions obtained have been consequently validated with a comparison with these reference data, see e.g. the careful validation of the R3 solution reported in Ref. 28. A study of the numerical convergence of the present simulations is reported in appendix A while a general assessment of the effects of the domain spanwise length and of the mesh resolution can be found in Ref. 34.

After reaching a statistical steady state, the simulations have been run for 300 characteristic time scales D/U_∞ in order to obtain a number of sampling sufficient for statistical convergence. For the symmetry of the problem, statistics, hereafter denoted as $\langle \cdot \rangle$, are computed by averaging in time and in the spanwise direction. Finally, the customary Reynolds decomposition of the flow in a mean and fluctuating part, $u_i = U_i + u_i'$ and $p = P + p'$, will be hereafter used where the index $i = 1, 2, 3$ corresponds to the streamwise (x), vertical (y) and spanwise (z) directions of a reference Cartesian system centred at the beginning of the top flat wall as shown in figure 1. Throughout the paper, non-dimensional variables will be used, implying normalization of lengths with the plate thickness D and of velocities with the free-stream velocity U_∞.

III. INSTANTANEOUS FLOW REALIZATIONS

We start the analysis by considering the instantaneous flow pattern realized by the different flow configurations. To this aim we consider the eduction scheme proposed by Jeong *et al.* 35 and based on the second largest eigenvalue λ_2 of the tensor

$$\mathscr{T}_{ij} = S_{ik}S_{kj} + \Omega_{ik}\Omega_{kj} \tag{1}$$

where

$$S_{ij} = \frac{1}{2}\left(\frac{\partial u_i}{\partial x_j} + \frac{\partial u_j}{\partial x_i}\right)$$
$$\Omega_{ij} = \frac{1}{2}\left(\frac{\partial u_i}{\partial x_j} - \frac{\partial u_j}{\partial x_i}\right) \tag{2}$$

are the symmetric and antisymmetric part of the velocity gradient tensor. This eduction scheme is known to accurately extract the three-dimensional pattern of vortical structures. As shown by the iso-surface of $\lambda_2 = -4$ colored by the streamwise velocity in figure 2, the considered separated and reattaching flows exhibit a rather complex behaviour. The general behaviour shared by all the configurations consists of a detachment of an initially laminar shear layer highlighted by the flat iso-surface of λ_2 in the leading-edge region. Then, in a very short length, the separated flow develops large spanwise vortex tubes typical of the Kelvin-Helmholtz instability. Such large-scale structures further develop downstream

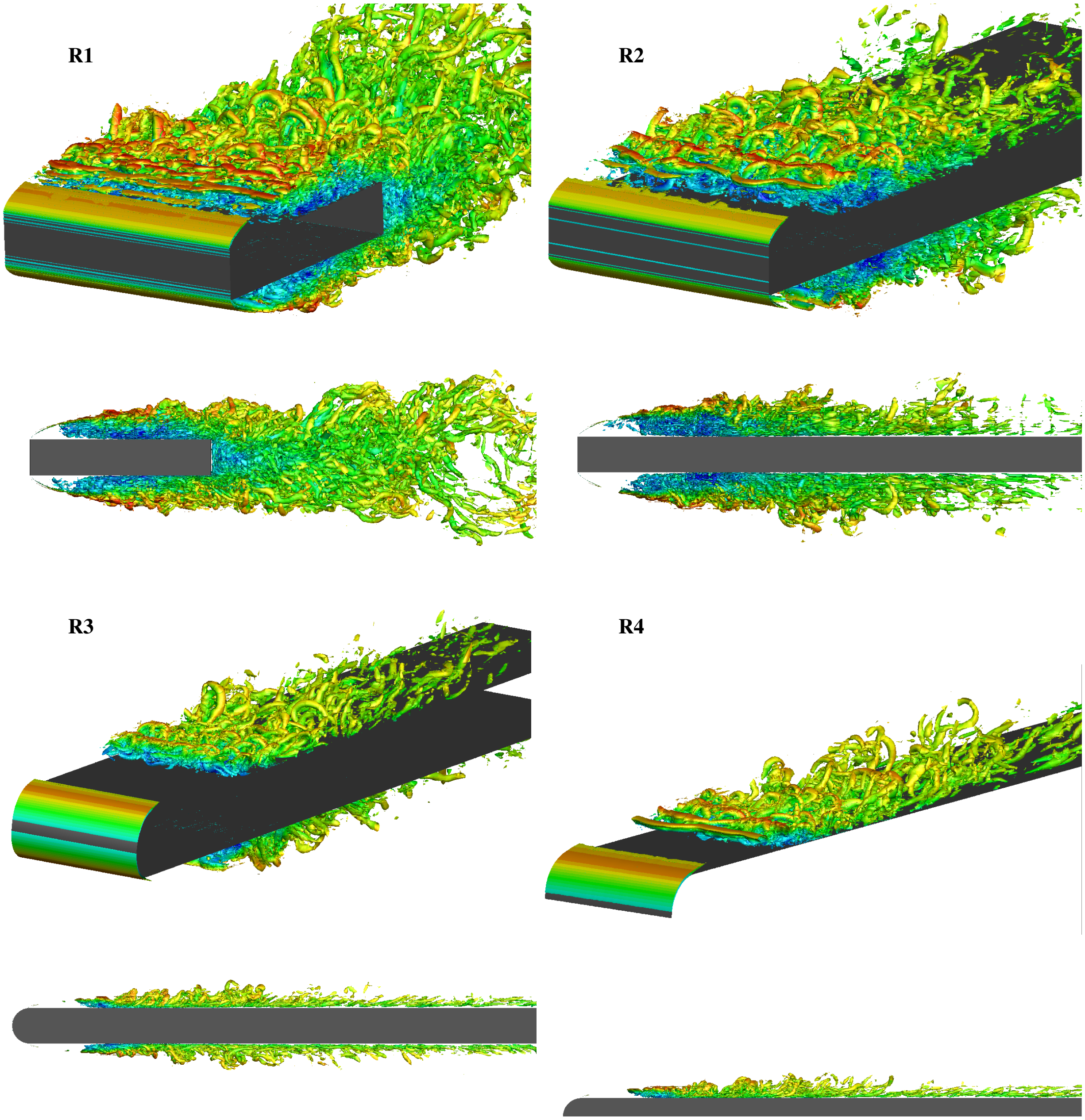

FIG. 2. Instantaneous flow realization of the different flow configurations simulated. Iso-surface of $\lambda_2 = -4$ colored by the streamwise velocity.

and, by interacting with shear, undergo a lift up in the vertical direction and stretching in the streamwise one thus forming hairpin-like structures[6,36]. This is the last stage before the development of fully turbulent regime composed by turbulent structures arranged in a chaotic manner. Besides the obvious differences due to the downstream presence of a wake or of a flat boundary layer, the main difference between the different flow configurations concerns small scale fluctuations. In particular, it seems that flows with right-angle corners develop a wider range of turbulence fluctuations. Indeed, as shown in figure 2, R1 and R2 appear to be populated by a variety of small scale fluctuations superimposed to a large scale velocity field whose characteristics are shared by the different configurations analysed.

In order to quantitatively assess the multiscale features of the analysed flows, we make use of frequency spectra of vertical velocity defined as,

$$E_{vv}(x,y,St) = \langle \hat{v}(x,y,St)\hat{v}^*(x,y,St) \rangle \tag{3}$$

where $St = fD/U_\infty$ is the Strouhal number with f the frequency and $(\hat{\cdot})$ denotes the Fourier transform with respect to time. In figure 3, the evolution of the premultiplied frequency spectra along the shear layer for the different flow configurations is shown. It is evident that in all the cases, the range of

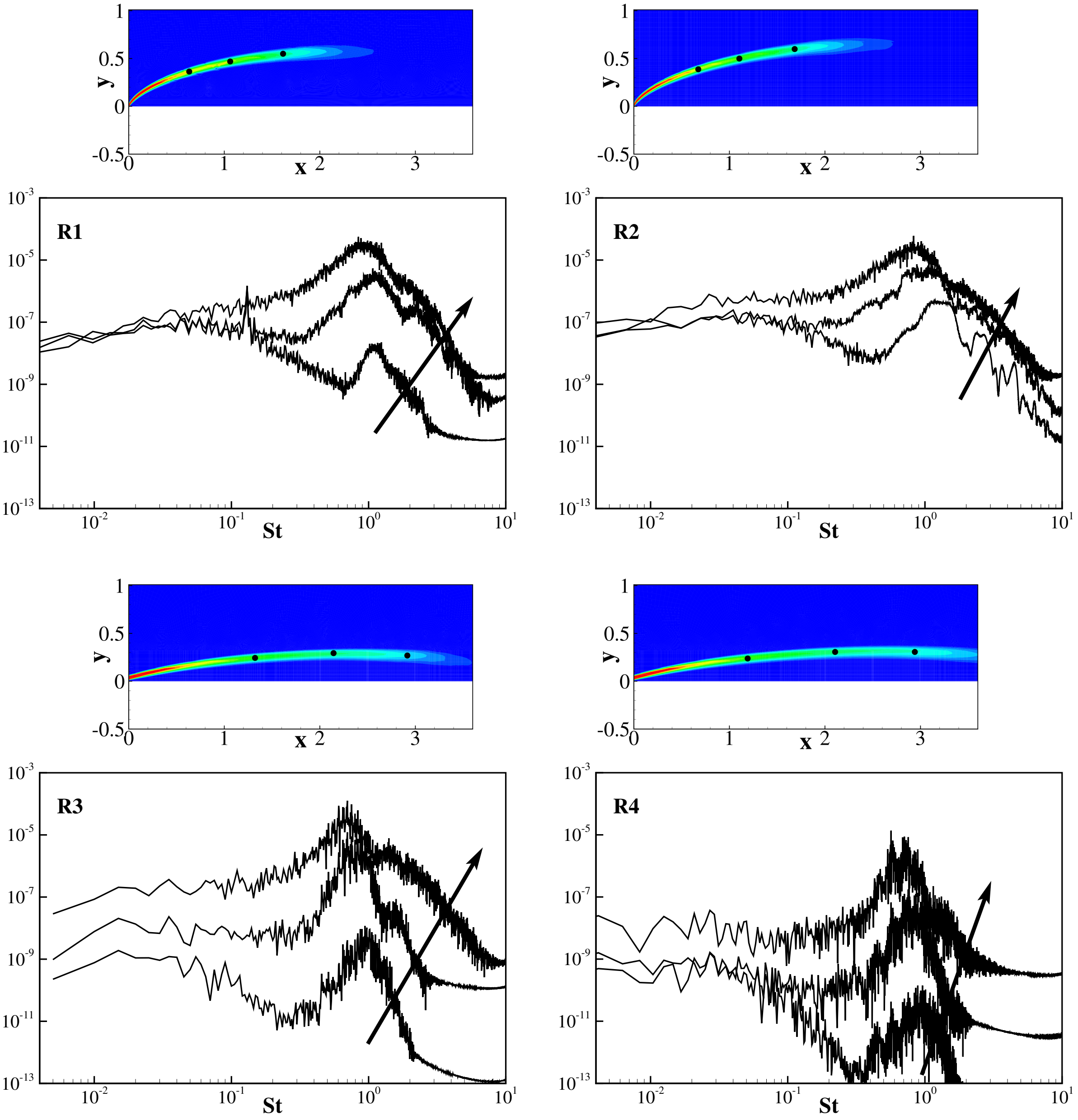

FIG. 3. Premultiplied frequency spectrum of vertical velocity $St\,E_{vv}(St)$ computed along the leading-edge shear layer for the different flow configurations simulated. The arrows indicate increasing streamwise locations. On top of each spectrum, the iso-contours of $\partial U/\partial y$ are shown to highlight the location of the leading-edge shear layer and the positions of the probes used to compute the spectra.

frequencies amplified by the transitional mechanisms of the shear layer are centred at $St \approx 1$. This amplification leads to a fill up of the entire spectrum that is particularly evident for the flow cases with right-angle corners in accordance with the instantaneous flow topology analysed so far. The premultiplied frequency spectra allow us also to analyse the low-frequency unsteadinesses of the flow[1]. Being associated with the instability of the entire recirculating region, its statistical footprint is expected to be present at very small frequencies and to be almost independent on the position considered since the associated very large-scale motions should be felt almost everywhere in the flow. As shown in figure 3, this type of statistical footprint is present only in flow cases with right-angle corners (R1 and R2). In accordance with Cimarelli *et al.* 9, the range of frequencies is centred at $St \approx 0.05$. Their intensity is significant at all positions along the measured points in the leading-edge shear layer thus supporting the idea that the energy related with these frequencies is associated with an unsteady phenomenon involving the entire flow recirculation[1,36] and, hence, is felt almost everywhere. All these aspects are not apparent for the smooth corner cases (R3 and R4). Indeed, a well-defined central frequency is absent since the spectral behaviour at low frequencies is found to be largely modulated throughout the shear layer development thus suggesting

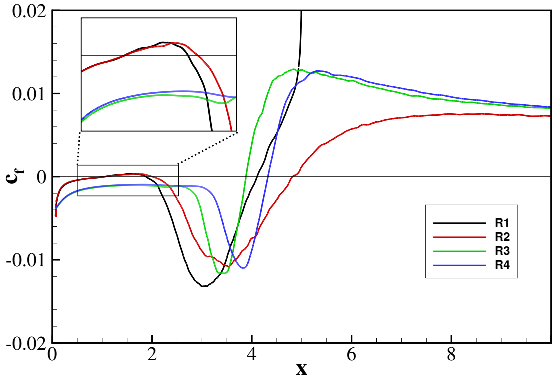

FIG. 4. Streamwise behaviour of the friction coefficient for the different flow configurations simulated.

that the energy content of these low frequencies is associated with motions that do not involve the entire flow recirculation. Hence, the very slow unsteadiness phenomena of the entire flow recirculation appear to be peculiar mechanisms of plates with sharp corners. We argue that such a distinction in reproducing a very low-frequency unsteadiness is related with the height of the recirculating bubble that, as it will be shown in the next section, is significantly higher in flows with right-angle corners thus promoting the instability of the entire recirculating region. In closing this section, let us notice also the effect of trailing-edge flow separation. By comparing flow cases R1 and R2, it is evident the appearance of the shedding frequency $St \approx 0.14$ for the case R1. As shown in Cimarelli *et al.* 36, the motion associated with the vortex shedding superimpose to that slower of the recirculating bubble thus forming a self-sustaining cycle.

IV. FRICTION AND PRESSURE COEFFICIENTS

We start the statistical analysis of the flow by considering first wall quantities. As shown in figure 4, the behaviour of the friction coefficient, c_f, highlights significant differences between the different flows. The general trend of the friction coefficient conforms with the presence of a large scale recirculating region $c_f < 0$ followed by an attached forward boundary layer $c_f > 0$. The main differences between the different flow configurations come from the length of the main recirculating region and from the presence or not of a second smaller recirculating flow within it.

Starting from the last consideration, we observe that for the flow cases with right angle corners, R1 and R2, the near-wall reverse flow induced by the large scale recirculating bubble, detaches forming a secondary smaller recirculation that can be recognized by the presence of positive values of friction for streamwise locations within the main separation bubble, see the inset in figure 4. In both cases, the secondary bubble starts around $x = 1.04$, however its length ℓ_{sv} is found to be slightly larger for the case of an infinite plate R2. This secondary flow is not observed for the cases with circular leading-edge corner, R3 and R4. As shown in Cimarelli *et al.* 36, the presence of the secondary vortex is a result of adverse pressure gradient phenomena which induce the separation of the reverse boundary layer produced by the main recirculating flow. Accordingly, as shown in figure 5(a), the pressure coefficient highlights a negative streamwise gradient, $dc_p/dx < 0$, only for the flow cases with right angle corners R1 and R2. Hence, only for these two flow cases, the reverse flow induced by the main recirculating bubble experiences an adverse pressure gradient. As a consequence, the reverse boundary layer detaches, thus leading to a secondary smaller recirculating region.

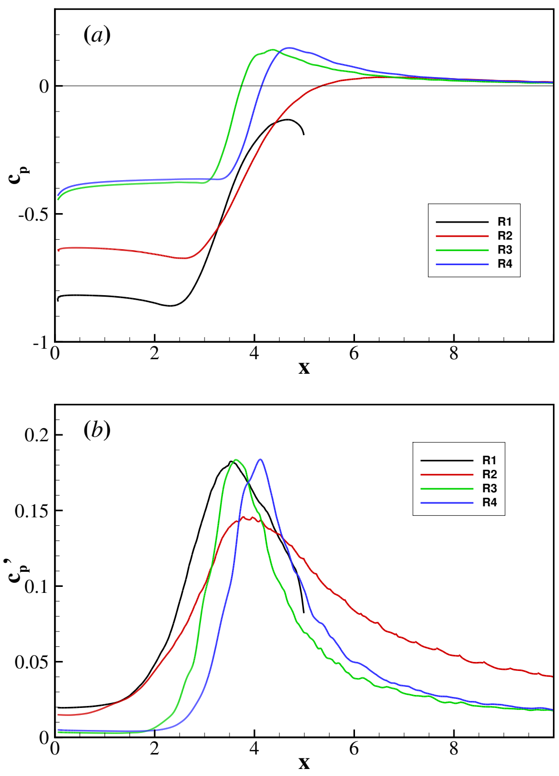

FIG. 5. Streamwise behaviour of the pressure coefficient (a) and of its standard deviation (b) for the different flow configurations simulated.

As far as it concerns the length of the main recirculating region, we observe that all the flow cases behave in a different way. The reattachment length strongly depends on the turbulence levels created in the leading-edge shear layer which in turn are affected by the geometry of the leading-edge corner and by the presence/absence of trailing edge vortex shedding mechanisms as unequivocally shown here in quantitative terms.

It is worth pointing out that, as expected, in the upstream portion of the flat plates, the behaviour of the friction coefficient appears to be strongly affected by the geometry of the leading edge independently of the presence or not of a trailing edge flow separation. Indeed, similar behaviours are observed for the same geometry. On the other hand, while moving downstream, the effect of the presence of the trailing-edge separation becomes relevant and a departure of the behaviour of the friction coefficient for the cases R1 and R2 is observed. Interestingly, when comparing cases R3 and R4, one would expect that the effect of the presence/absence of a flow separation in the two sides of the plate is more relevant in the region close to the leading edge where the top and bottom sides of the plate communicate. However, as shown here in quantitative terms, the effect of the presence/absence of a flow separation in the two sides of the plate is negligible in the upstream part of the plate where the friction coefficient shows similar behaviour and a significant departure is observed only downstream. The same reasoning applies when comparing the downstream behaviour of the friction coefficient of flow cases R2 and R3. Indeed, we would expect that the effect of the different leading-edge geometry is retained only in the upstream part of the plate. On the contrary, the differences are observed also downstream.

Let us consider now the behaviour of the pressure coefficient c_p and of its standard deviation c'_p shown in figure 5(a) and (b), respectively. As for the friction coefficient analysed so far, the leading-edge geometry is the most significant parameter influencing the upstream behaviour of the recirculating flow. Indeed, we observe that, both in terms of average and fluctuating intensity, the pressure field behaves similarly for the flow cases R1/R2 and R3/R4. It consists in a flat behaviour of c_p associated with small value of c'_p for the circular leading-edge geometry. On the other hand, for right-angle corners, the pressure field c_p slightly decreases moving downstream the leading edge, $dc_p/dx < 0$, and the associated fluctuations, c'_p are more intense. Let us recall that, as previously shown when analysing the behaviour of the friction coefficient, the presence of a negative pressure gradient, $dc_p/dx < 0$, is at the basis of the formation of the secondary recirculating flow.

By moving downstream, the pressure recovery show significant differences which are particularly interesting for the flow cases without trailing edge separation, i.e. R2, R3 and R4. Indeed, these flow cases differentiate for the geometry of the leading edge corner and for the presence or not of flow separation in the two sides of the plate. Such differences are physically located upstream but their effects are significant also in the pressure recovery region downstream the reattachment. Indeed, an homogenization of the pressure distribution between the different cases is recovered for $x > 7$ only for c_p.

V. MEAN VELOCITY FIELD AND TURBULENT KINETIC ENERGY

The behaviour of the mean velocity field for the different flow configurations is shown in figure 6 with streamlines. We observe that the main recirculating region is strongly affected by the shape of the leading-edge corner. Indeed, sharp leading-edge corners, R1 and R2, are found to produce thicker recirculating bubbles with respect to circular leading-edge corners. This aspect could be at the basis of the very-slow frequency unsteadiness observed only for right-angle corner flows as shown in section §III. The effect of the trailing-edge separation consists in a reduction of the average length of the recirculating zone, compare R1 and R2. On the other hand,

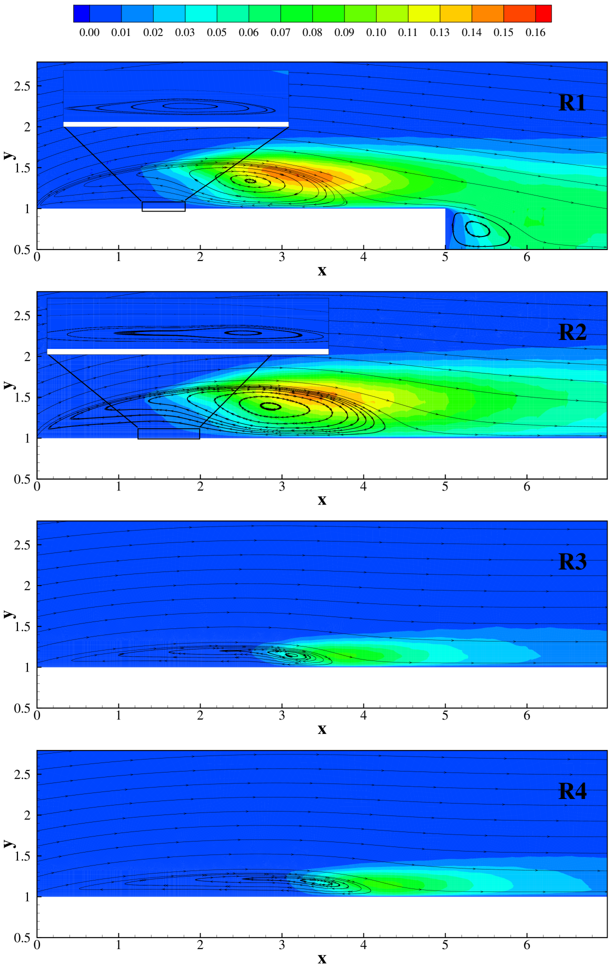

FIG. 6. Mean velocity field streamlines and iso-contours of turbulent kinetic energy $q(x,y)$.

by comparing R3 and R4, we observe that the effect of coupling phenomena between the two sides of the plate is less significant as far as it concerns the height of the recirculating flow. On the contrary, as far as it concerns the length of the recirculating flow, a significant streamwise elongation is observed when coupling phenomena between the two sides are precluded, see the behaviour of the friction coefficient in figure 4.

Interesting insights can be argued by analysing the behaviour of the turbulent kinetic energy, $q(x,y) = \langle u'_i u'_i \rangle/2$, shown with iso-contours in figure 6 for the different flow configurations. It is evident how the presence of a sharp leading-edge corner, beside producing a thicker flow recirculation, leads to a faster transition to turbulence. Indeed, the initially laminar leading-edge shear layer is found to develop instabilities and turbulence fluctuations for streamwise locations which are significantly upstream for the case of sharp leading-edge corners with respect to the smooth ones, compare the turbulent intensity levels of cases R1 and R2 to the cases R3 and R4. This upstream shift of the main instabilities giving rise to turbulent transition is associated also to more intense turbulent fluctuations. Indeed, for all the flow cases, the most intense fluctuations are reached in the shedding region of the main recirculating bubble but, as highlighted by the higher levels of the iso-contours, these maxima are stronger for flow with sharp leading-edge corners with respect to those with smooth corners.

VI. PRODUCTION OF TURBULENT FLUCTUATIONS

An important aspect of separating and reattaching flow is that production of turbulence fluctuations is embedded into the system rather than being provided by an external agent. To study this aspect it is useful to consider the budget equations for the Reynolds stresses, $\langle u_i'u_j'\rangle$. Such equations can be derived from the Navier-Stokes equations and read

$$\frac{\partial \langle u_i'u_j'\rangle}{\partial t} + \underbrace{\frac{\partial \langle u_i'u_j'\rangle U_k}{\partial x_k} + \frac{\partial \langle u_i'u_j'u_k'\rangle}{\partial x_k} + \frac{1}{\rho}\frac{\partial \langle p'u_j'\rangle}{\partial x_i} + \frac{1}{\rho}\frac{\partial \langle p'u_i'\rangle}{\partial x_j} - \nu\frac{\partial^2 \langle u_i'u_j'\rangle}{\partial x_k \partial x_k}}_{\partial \phi_k^{ij}/\partial x_k} = \underbrace{\frac{1}{\rho}\langle p'\left(\frac{\partial u_i'}{\partial x_j} + \frac{\partial u_j'}{\partial x_i}\right)\rangle}_{p^{ij}} \underbrace{-\langle u_i'u_k'\rangle\frac{\partial U_j}{\partial x_k} - \langle u_j'u_k'\rangle\frac{\partial U_i}{\partial x_k}}_{\Pi^{ij}} \underbrace{-2\nu\langle\frac{\partial u_i'}{\partial x_k}\frac{\partial u_j'}{\partial x_k}\rangle}_{\varepsilon^{ij}} \tag{4}$$

Equations (4) can be rewritten in a symbolic form as

$$\frac{\partial \langle u_i'u_j'\rangle}{\partial t} + \frac{\partial \phi_k^{ij}}{\partial x_k} = p^{ij} + \Pi^{ij} - \varepsilon^{ij} , \tag{5}$$

where we can recognize the transport of turbulent stresses within the flow domain, ϕ_k^{ij}, the local balance between production and dissipation processes, $\Pi^{ij} - \varepsilon^{ij}$, and the inter-component pressure-strain transfer of energy p^{ij}. For the statistical symmetries of planar separating and reattaching flow as those considered here, we have that $\partial\langle\cdot\rangle/\partial t = 0$ and $\partial\langle\cdot\rangle/\partial z = 0$, so that the above equations reduce to

$$\frac{\partial \phi_x^{ij}}{\partial x} + \frac{\partial \phi_y^{ij}}{\partial y} = p^{ij} + \Pi^{ij} - \varepsilon^{ij} , \tag{6}$$

thus highlighting that the transport of turbulent stresses statistical occurs only in the streamwise and vertical directions driven by a field of fluxes $(\phi_x^{ij}, \phi_y^{ij}, 0)$. In equation (6), the term Π^{ij} commonly represents a source of turbulence, $\Pi^{ij} > 0$. It extracts energy from the mean field to sustain the transport $(\phi_x^{ij}, \phi_y^{ij}, 0)$ and redistribution p^{ij} processes down to dissipation ε^{ij}. For this reason Π^{ij} is commonly called turbulence production term. By considering only the diagonal terms of the turbulent stresses, i.e. twice the kinetic energy of each component of the fluctuating velocity field, and considering again the statistical symmetries of the flow, the production term is active only for the streamwise and vertical velocity components, i.e.

$$\Pi^{11} = -2\langle u'u'\rangle\frac{\partial U}{\partial x} - 2\langle u'v'\rangle\frac{\partial U}{\partial y} \tag{7}$$

$$\Pi^{22} = -2\langle v'v'\rangle\frac{\partial V}{\partial y} - 2\langle u'v'\rangle\frac{\partial V}{\partial x} \tag{8}$$

$$\Pi^{33} = 0 . \tag{9}$$

Accordingly, to study how turbulence fluctuations are produced in separating and reattaching flows, in what follows, we will consider the behaviour of the production terms Π^{11} and Π^{22}.

A. Production of streamwise turbulent fluctuations

In figure 7, the iso-contours of Π^{11} for the different flow configurations are shown. It is evident that production of streamwise fluctuations is active also along the leading-edge shear layer in the case of sharp corners R1 and R2, while, in the case of smooth corners R3 and R4, production is present only in the shedding region of the recirculating bubble. A slight increase of the production levels is also observed in the case of sharp corners. In this context, the effect of the presence of a flow separation at the trailing edge is to induce a further significant increase of the intensity of the production mechanisms of streamwise fluctuations, compare R1 with R2. The previously observed behaviours of turbulent kinetic energy, figure 6, are consistent with and could be ascribed to the upstream estention and to the increase of the production of streamwise fluctuations in the case of sharp corners and even more with the presence also of trailing-edge separation.

Interestingly, figure 7 highlights the presence also of regions of reversal of flow energy from the fluctuating to the mean streamwise velocity field. Indeed, in the reattachment region of the flow we observe negative values of production, $\Pi^{11} < 0$. This phenomenon is observed in all the flow configurations considered and can be attributed to the wall-impinging of flow structures that on average mainly occurs in this region of the flow. Indeed, due to impinging, pressure-strain phenomena p^{ij} redistribute the kinetic energy of vertical fluctuations to the horizontal velocity components, thus, leading to a highly oscillatory streamwise velocity behaviour in the wall region which alternatively promote the development of an upstream and downstream boundary layer, see Cimarelli *et al.* 36. Accordingly, from the inspection of the data, these reverse flow phenomena $\Pi^{11} = -2\langle u'u'\rangle\partial U/\partial x - 2\langle u'v'\rangle\partial U/\partial y < 0$ are found to be essentially due to the term $-2\langle u'u'\rangle(\partial U/\partial x)$ and hence to the divergent behaviour of the mean streamwise velocity field in this region of the flow, i.e. $\partial U/\partial x > 0$.

B. Production of vertical turbulent fluctuations

In figure 8, the iso-contours of Π^{22} for the different flow configurations are shown. Apparently, the production of vertical fluctuations, $\Pi^{22} > 0$, is significantly active only in the

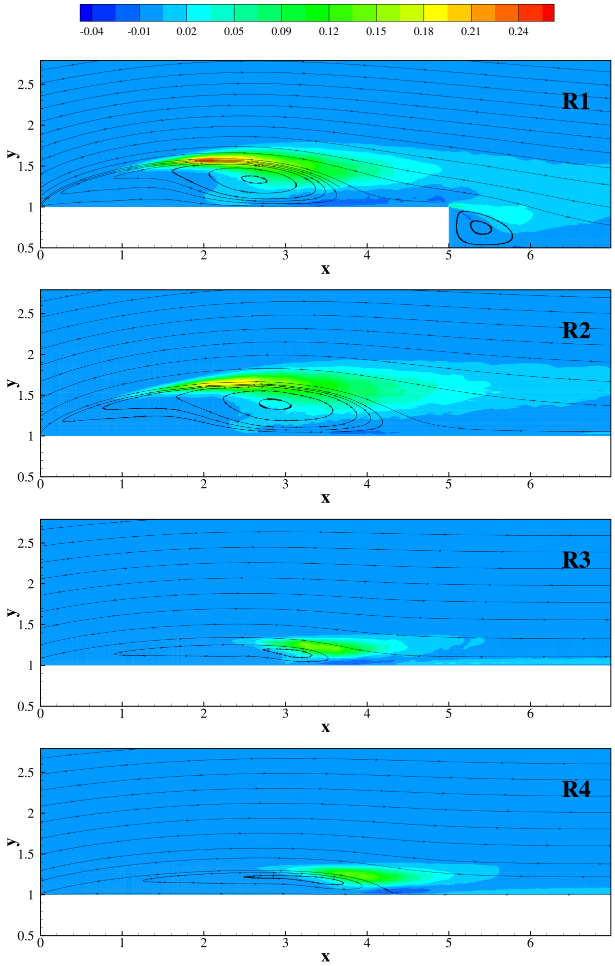

FIG. 7. Mean velocity field streamlines and iso-contours of production of streamwise fluctuations, $\Pi^{11}(x,y)$.

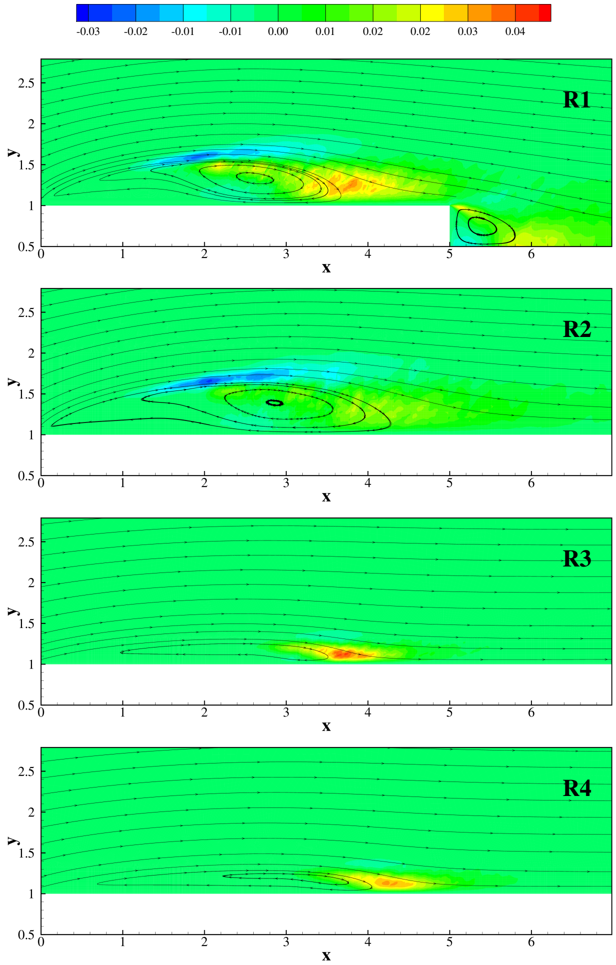

FIG. 8. Mean velocity field streamlines and iso-contours of production of vertical fluctuations, $\Pi^{22}(x,y)$.

shedding region of the recirculating bubble for all the flow configurations considered. The only difference comes from the intensity of the process which is found to be significantly reduced when sharp corners are combined with a downstream development of a flat boundary layer, compare R2 with respect to the other flow cases.

Interestingly, intense phenomena of reversal of flow energy from the fluctuating to the mean vertical velocity field, $\Pi^{22} < 0$, are present. As shown in figure 8, these phenomena take place along the development of the leading-edge shear layer and only for the flow cases with sharp corners, R1 and R2. Contrary to those observed for the streamwise velocity field, these negative production mechanisms are intense as much as those of positive turbulence production. From the inspection of the data, we found that both terms composing the production of vertical fluctuations, $\Pi^{22} = -2\langle v'v'\rangle \partial V/\partial y - 2\langle u'v'\rangle \partial V/\partial x$, contribute to the negative value of Π^{22} in this region of the flow thus highlighting that both a divergent behaviour of the mean vertical velocity field $\partial V/\partial y > 0$ and a positive correlation of Reynolds shear stresses $\langle u'v'\rangle$ and streamwise shear $\partial V/\partial x$ contribute to the reversal of flow energy from the fluctuating to the mean vertical velocity field. Being a peculiar mechanisms of sharp leading-edge corners, we conjecture that negative production mechanisms of vertical fluctuations in the leading-edge shear layer could be responsible, at least partially, to the development of a thicker recirculating region in such a flow cases. In fact, negative production phenomena correspond to a production of mean vertical velocity.

C. On negative production of turbulent kinetic energy

As shown in Cimarelli *et al.* 37, negative production phenomena of turbulent kinetic energy,

$$tr(\Pi^{ij})/2 = -\left(\langle u'^2\rangle - \langle v'^2\rangle\right)\frac{\partial U}{\partial x} - \langle u'v'\rangle\left(\frac{\partial U}{\partial y} + \frac{\partial V}{\partial x}\right) \tag{10}$$

are found to occur in the leading-edge shear layer of the flow around a rectangular plate with sharp leading and trailing edges. The presence of these phenomena are shown to be a challenge for turbulence theories that should predict a source of mean kinetic energy from the interaction of turbu-

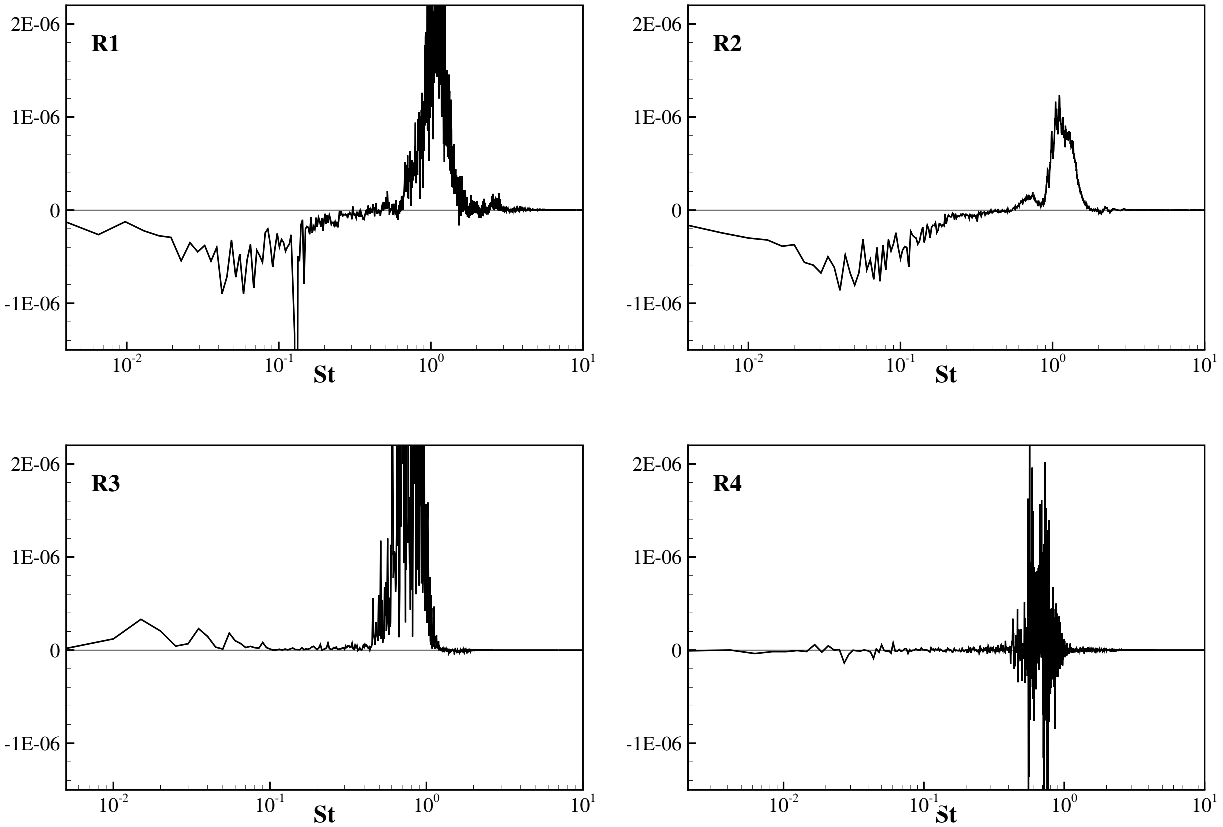

FIG. 9. Premultiplied frequency cospectrum $St\,E_{-uv}(St)$ computed in the leading-edge shear layer for the different flow configurations simulated. The exact location of the probe is reported in figure 3.

lent stresses and mean velocity gradients. This fact is of overwhelming importance also for turbulence closures as shown in Cimarelli *et al.* 38 in a context of Large Eddy Simulation. As shown in Cimarelli *et al.* 37, negative turbulence production phenomena are given by the negative value of the Reynolds shear stresses in the shear layer, $-\langle u'v'\rangle$. In particular, the phenomena determining the sign of the Reynolds shear stresses in the shear layer, $-\langle u'v'\rangle$, are found in Cimarelli *et al.* 37 to be related with the motions induced by the very-large scale unsteadiness of the entire flow recirculation.

As already reported in section §III, premultiplied frequency spectra of vertical velocity show that this very-slow phenomenon is typical of the flow cases with right-angle corners, thus, explaining the presence of negative turbulence production phenomena in such flows and their absence in the flow cases with smooth corners. To verify this conjecture, in figure 9, the premultiplied frequency cospectra, $St\,E_{-uv}(St)$, evaluated along the leading-edge shear layer are reported. It is evident that for the flow cases with right-angle corners, R1 and R2, the cospectrum show two-distinct behaviours contributing to the Reynolds shear stresses $-\langle u'v'\rangle$ with opposite sign. In particular, a range of small time scales centred at $St \approx 1$ is found to produce positive turbulent stresses, $-\langle u'v'\rangle > 0$, while a range of very slow scale motion centred at $St \approx 0.05$ is found to produce negative turbulent stresses, $-\langle u'v'\rangle < 0$. As shown in section §III, the former is a range of small-scale fluctuations that are amplified along the shear layer by transitional mechanisms thus leading to turbulence. On the other hand, the latter range of very slow motions is related with the instability of the entire recirculating region. As shown here in quantitative terms, this very slow motion is the origin of the negative turbulence production mechanisms in the shear layer of flows with right-angle corners, R1 and R2. On the other hand, as shown in section §III, the flow cases with smooth corners are not characterized by this instability of the entire recirculating bubble. Accordingly, the relative premultiplied frequency cospectra, shown in figure 9 (cases R3 and R4), do not exhibit the large scale negative contribution to the turbulent stresses thus explaining the absence of negative turbulence production phenomena. Indeed, only the small scale contribution due to the development of turbulence survives thus leading solely to classical positive turbulence production mechanisms.

VII. SENSITIVITY TO FREE-STREAM TURBULENCE

In the present section we address how the different flow configurations react to the presence of a non-zero free-stream turbulence level. To this aim, the four numerical cases described in section §II have been run again using the same numerical settings and adding a free-stream turbulence level $\sqrt{2q}/U_\infty = 0.002$. This very low but finite value of free-stream turbulence has been considered in order to study the sensitivity of the flow configurations on this parameter. Furthermore, it allows to reproduce the settings of the ERCOFTAC T3L test case experiments. In this respect, let us notice the good agreement of the present computations with the experimental data shown in Ref. 28 and 39

In the present work, due to mesh coarsening, the application of a free-stream turbulence at the inlet is unfeasible. Hence, turbulent fluctuations are introduced by applying a spatially-supported random forcing term to the momentum equations which is active in the regions of the flow just upstream the plates where the mesh density is enough to not dissipate them. The random forcing is homogeneous in the cross-flow (y,z)-plane and assumes a Gaussian distribution in the streamwise direction that is centred at $x=-3$. The width of the Gaussian distribution is 0.01 while the intensity of the forcing is adapted in the different flow configurations to obtain a free-stream turbulence level at the leading-edge of the plates $\sqrt{2q}/U_\infty = 0.002$, see Ref. 28 for more details.

In figure 10, the behaviour of the friction and pressure coefficients for the different flow configurations with and without free-stream turbulence are shown. Interestingly, the effects of free-stream turbulence are almost negligible for the flow configurations with right-angle corners, cases R1 and R2. Indeed, both the profiles with and without free-steam turbulence of the friction and pressure coefficient almost collapse each other for these flow cases. We argue that this lack of sensitivity on free-stream turbulence is due to the absorption effect of vertical fluctuations performed by the negative production mechanisms observed to occur in the shear layer for the flow cases with right-angle corners.

As shown in the previous section, such negative production phenomenon is induced by the very-slow motions related to the instability of the entire recirculating bubble that are found to be typical of flows with sharp leading-edge corners. Accordingly, in the flow cases with smooth leading-edge corners, negative production mechanisms are not observed and a strong sensitivity of the flow on the free-stream turbulence level is found as unequivocally shown in quantitative terms in figure 10. Indeed, despite the very small value of free-stream turbulence considered, the behaviour of the friction coefficient shows a drastic shortening of the recirculating region for both smooth corner cases R3 and R4, see Lamballais *et al.* 15 and 40 where similar features are reported. Interestingly, the effect of free-stream turbulence is to cancel out the effects related to the flow coupling between the top and bottom sides of the plate. In fact, the differences that were observed between the flow cases R3 and R4 without free-stream turbulence are cancelled by the addition of a very small value of free-stream turbulence. As shown in figure 10 the friction and pressure profiles of the flow cases R3 and R4 collapse in the case of free-stream turbulence.

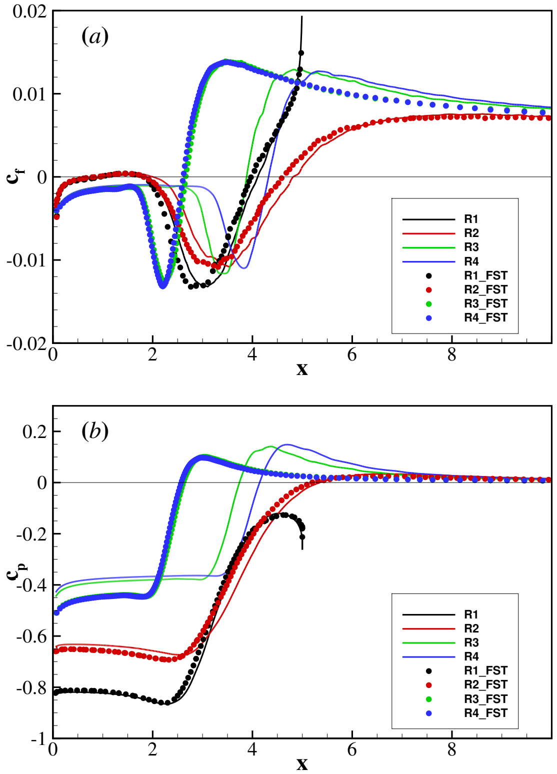

FIG. 10. Streamwise behaviour of the friction (a) and pressure (b) coefficients for the different flow configurations simulated with and without free-stream turbulence. The colours encode the flow configuration while circles denote the behaviour with free-stream turbulence and solid lines reports the profiles without free-stream turbulence.

VIII. FINAL DISCUSSIONS

In the present work, the ability of numerical simulations to manipulate the flow conditions in order to understand how geometrically relevant parameters influence the behaviour of separating and reattaching flows is exploited. In particular, the effect of the leading-edge corner geometry (sharp and smooth), of the trailing-edge flow separation and of the flow coupling between the top and bottom sides of the plate are investigated by means of four different flow configurations: the flow around a finite rectangular plate with right-angle corners (R1), the flow around an infinite plate with right-angle leading-edge corner (R2), the flow around an infinite flat plate with circular leading-edge corner (R3) and the flow occurring solely in the top side of an infinite flat plate with circular leading-edge corner (R4). For the solution of these flow problems, implicit LES simulations have been performed by using a high-order Discontinuous Galerkin numerical method.

The results reveal that the most significant differences between the different flow configurations are, in general, given by the geometry of the leading-edge corner. However, secondary differences given by the presence of a trailing-edge separation or by a coupling between the top and bottom sides of the plate are found and analysed in detail. Here, we resume only the main results.

We found that the flow configurations with right-angle corners are characterized by a thicker recirculating bubble and by the presence of a secondary smaller recirculation within it. This secondary flow is given by a negative streamwise pressure gradient $dc_p/dx < 0$ that acts as adverse pressure gradient for the reverse boundary layer induced by the main recirculation thus promoting its separation and leading to the secondary recirculation. The right-angle corner cases are also found to develop higher turbulence intensities as a result of an increased level of turbulence production of streamwise fluctuations.

The spectral analysis of the flows reveals that the fluctuations amplified by the transitional mechanisms of the shear layer lie in the same range of frequencies for all the flow cases that is centred at $St \approx 1$. The main difference between the different flow configurations is given by the fact that a very-slow frequency unsteadiness of the recirculating bubble, centred at $St \approx 0.05$, appears in separating flows with right-angle corners. We argue that this large-scale instability of the entire recirculating bubble is related to the height of the flow recirculation itself that is, in fact, very large in the case of right-angle corners with respect to smooth corners. This aspect gives rise to the question if there exists a critical height for the development of the bubble instability mechanisms.

The presence of a very-large scale unsteadiness of the main recirculating bubble has strong consequences on the behaviour of the separating and reattaching flow. Indeed, the analysis of the frequency cospectra reveals that this large scale unsteadiness is responsible for negative turbulence production phenomena of vertical fluctuations in the leading-edge shear layer. This reversal of flow energy from the fluctuating to the mean vertical velocity field is argued to be at the basis of the development of thicker recirculating region in sharp-edges flows. Overall, the picture is that of a source of mean vertical velocity at the leading-edge shear layer that leads to thick flow recirculations whose height exceeds a critical limit for the development of very low-frequency instabilities of the entire recirculating bubble that in turn are responsible for the leading-edge negative production itself thus closing a self-sustained cycle.

This negative production of vertical fluctuations as strong consequences also for the sensitivity of the flow on the presence of a free-stream turbulence level. Indeed, negative production is found to absorb free-stream fluctuations thus leading to a weak sensitivity of the flow cases with right-angel corners to the presence of free-stream turbulence. On the contrary, in smooth corner cases this phenomenon is absent and a stronger sensitivity to free-stream turbulence is observed which leads to a drastic shortening of the flow recirculation.

Data availability. The data that support the findings of this study are available from the corresponding author upon reasonable request.

ACKNOWLEDGMENTS

We would like to acknowledge Pierangelo Conti and Adriano Leonforte who help us in the design of the numerical settings of the R1 test case.

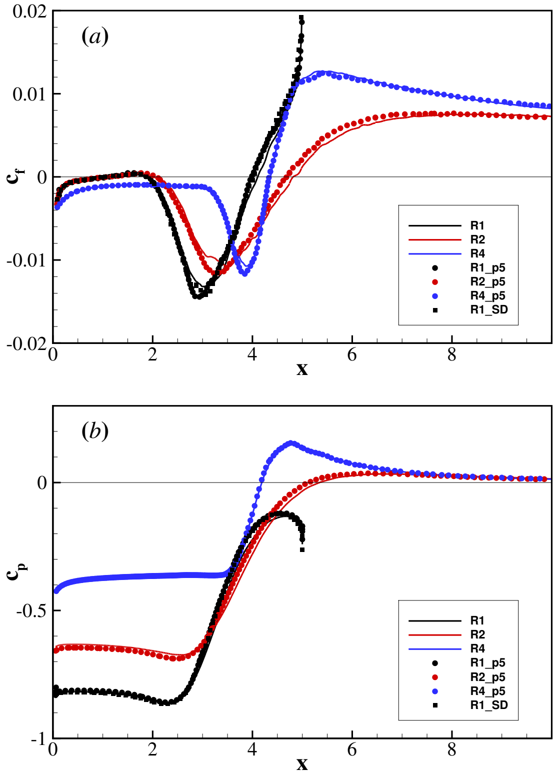

FIG. 11. Streamwise behaviour of the friction (a) and pressure (b) coefficients for different flow configurations encoded by colours and numerical settings encoded by symbols.

Appendix A: Numerical convergence

The first requirement of the Large Eddy Simulation approach is to correctly reproduce first order moment statistics regardless of the resolution adopted. To verify that the DG-based implicit LES approach here adopted satisfies this requirement, we compare the statistical behaviour of the friction and pressure coefficients obtained using a fifth order polynomial representation (flow cases R1_p5, R2_p5 and R4_p5) with those analysed in the paper (flow cases R1, R2 and R4) corresponding to a sixth order polynomial representation. This reduction of the polynomial order corresponds to a reduction of resolution that in terms of degrees of freedom is 20%. To further assess the robustness of the approach employed, for the finite rectangular plate case we also address the convergence of the statistics by varying the top and bottom boundary conditions from free-stream to a symmetry condition and the numerical domain dimensions as well as the time step size. The additional simulation (case R1_SD) employing such variations is hence compared with that analysed in the paper (case R1). The overall numerical parameters of the additional simulation tests are reported in table II. As shown in figure 11, the numerical method employed highlights a robustness of first order moment statistics to variations of these numerical parameters.

.

Case	Re	$\mathscr{L}_x$	$\mathscr{D}_x \times \mathscr{D}_y \times \mathscr{D}_z$	N_e	DoF	Δy	Δz	Δt
R1_p5	3000	72	$200 \times 151 \times 5$	52695	$3.5 \cdot 10^6$	0.0046	0.082	0.025
R2_p5	3000	20	$36 \times 50 \times 5$	29538	$2 \cdot 10^6$	0.0042	0.136	0.05
R4_p5	3450	12	$28 \times 8.5 \times 2$	18820	$1.3 \cdot 10^6$	0.0025	0.049	0.05
R1_SD	3000	35	$112 \times 50 \times 5$	47670	$4 \cdot 10^6$	0.0039	0.049	0.05

TABLE II. Parameters of the test simulations used to verify the robustness of the numerical method. See the caption of table I.

[1] M. Kiya and K. Sasaki, "Structure of large-scale vortices and unsteady reverse flow in the reattaching zone of a turbulent separation bubble," J. Fluid Mech. **154**, 463–491 (1985).

[2] D. M. Moore, C. K. Letchford, and M. Amitay, "Energetic scales in a bluff body shear layer," J. Fluid Mech. **875**, 543–575 (2019).

[3] A. N. Stokes and M. C. Welsh, "Flow-resonant sound interaction in a duct containing a plate, ii: square leading edge," J. Sound Vib. **104**, 55–73 (1986).

[4] Y. Nakamura, Y. Ohya, and H. Tsuruta, "Experiments on vortex shedding from flat plates with square leading and trailing edges," J. Fluid Mech. **222**, 437–447 (1991).

[5] Y. Ohya, Y. Nakamura, S. Ozono, H. Tsuruta, and R. Nakayama, "A numerical study of vortex shedding from flat plates with square leading and trailing edges," J. Fluid Mech. **236**, 445–460 (1992).

[6] K. Hourigan, M. C. Thompson, and B. T. Tan, "Self-sustained oscillations in flows around long blunt plates," J. Fluids Struct. **15**, 387–398 (2001).

[7] R. Mills, J. Sheridan, and K. Hourigan, "Particle image velocimetry and visualization of natural and forced flow around rectangular cylinders," J. Fluid Mech. **478**, 299–323 (2003).

[8] L. Bruno, M. V. Salvetti, and F. Ricciardelli, "Benchmark on the aerodynamics of a rectangular 5: 1 cylinder: an overview after the first four years of activity," J. Wind Eng. Ind. Aerodyn. **126**, 87–106 (2014).

[9] A. Cimarelli, A. Leonforte, and D. Angeli, "Direct numerical simulation of the flow around a rectangular cylinder at a moderately high Reynolds number," J. Wind Eng. Ind. Aerodyn. **174**, 39–49 (2018).

[10] M. Kiya and K. Sasaki, "Structure of a turbulent separation bubble," J. Fluid Mech. **137**, 83–113 (1983).

[11] N. J. Cherry, R. Hillier, and M. E. M. Latour, "Unsteady measurements in a separated and reattaching flow," J. Fluid Mech. **144**, 13–46 (1984).

[12] K. Sasaki and M. Kiya, "Three-dimensional vortex structure in a leading-edge separation bubble at moderate reynolds numbers," J. Fluids Eng. **113**, 405–410 (1991).

[13] Z. Yang and P. R. Voke, "Large-eddy simulation of boundary-layer separation andtransition at a change of surface curvature," J. Fluid Mech. **439**, 305–333 (2001).

[14] M. Langari and Z. Yang, "Numerical study of the primary instability in a separated boundary layer transition under elevated free-stream turbulence," Phys. Fluids **25**, 074106 (2013).

[15] E. Lamballais, J. Silvestrini, and S. Laizet, "Direct numerical simulation of flow separation behind a rounded leading edge: Study of curvature effects," Int. J. Heat Fluid Flow **31**, 295–306 (2010).

[16] B. Rocchio, A. Mariotti, and M. V. Salvetti, "Flow around a 5:1 rectangular cylinder: Effects of upstream-edge rounding," J. Wind Eng. Ind. Aerodyn. **204** (2020).

[17] R. Hillier and N. J. Cherry, "The effects of stream turbulence on separation bubbles," J. Wind Eng. Ind. Aerodyn. **8**, 49–58 (1981).

[18] P. Saathoff and W. Melbourne, "Effects of free-stream turbulence on surface pressure fluctuations in a separation bubble," J. Fluid Mech. **337**, 1–24 (1997).

[19] Z. Yang and I. E. Abdalla, "Effects of free-stream turbulence on a transitional separated–reattached flow over a flat plate with a sharp leading edge," Int. J. Heat Fluid Flow **30**, 1026–1035 (2009).

[20] M. Ricci, L. Patruno, S. de Miranda, and F. Ubertini, "Flow field around a 5:1 rectangular cylinder using LES: Influence of inflow turbulence conditions, spanwise domain size and their interaction," Comput. Fluids **149**, 181–193 (2017).

[21] C. Mannini, A. M. Marra, L. Pigolotti, and G. Bartoli, "The effects of free-stream turbulence and angle of attack on the aerodynamics of a cylinder with rectangular 5:1 cross section," J. Wind Eng. Ind. Aerodyn. **161**, 42–58 (2017).

[22] G. Schewe, "Reynolds-number-effects in flow around a rectangular cylinder with aspect ratio 1:5," J. Fluid Struct. **39**, 15–26 (2013).

[23] F. Bassi, A. Crivellini, D. A. Di Pietro, and S. Rebay, "An implicit high-order discontinuous Galerkin method for steady and unsteady incompressible flows," Comput. Fluids **36**, 1529–1546 (2007).

[24] F. Bassi, A. Crivellini, D. A. Di Pietro, and S. Rebay, "An artificial compressibility flux for the discontinuous Galerkin solution of the incompressible Navier-Stokes equations," J. Comput. Phys. **218**, 794–815 (2006).

[25] A. Crivellini, V. D'Alessandro, and F. Bassi, "Assessment of a high-order discontinuous Galerkin method for incompressible three–dimensional Navier–Stokes equations: Benchmark results for the flow past a sphere up to Re=500," Comput. Fluids **86**, 442–458 (2013).

[26] F. Bassi, S. Rebay, G. Mariotti, S. Pedinotti, and M. Savini, "A high-order accurate discontinuous finite element method for inviscid and viscous turbomachinery flows." in *Proceedings of the 2nd European Conference on Turbomachinery Fluid Dynamics and Thermodynamics* (1997) pp. 99–108.

[27] J. Rang and L. Angermann, "New rosenbrock methods of order 3 for PDAEs of index 2," in *Proceedings of Equadiff-11 2005* (2007) pp. 385–394.

[28] M. Franciolini, L. Botti, A. Colombo, and A. Crivellini, "p-multigrid matrix-free discontinuous Galerkin solution strategies for the under-resolved simulation of incompressible turbulent flows," Comput. Fluids **206**, 104558 (2020).

[29] C. C. de Wiart, K. Hillewaert, L. Bricteux, and G. Winckelmans, "Implicit les of free and wall-bounded turbulent flows based on the discontinuous galerkin/symmetric interior penalty method," International Journal for Numerical Methods in Fluids **78**, 335–354 (2015).

[30] J.-B. Chapelier, M. [de la Llave Plata], F. Renac, and E. Lamballais, "Evaluation of a high-order discontinuous Galerkin method for the DNS of turbulent flows," Comput. Fluids **95**, 210 – 226 (2014).

[31] G. Gassner and A. Beck, "On the accuracy of high-order discretizations for underresolved turbulence simulations," Theor. Comput. Fluid Dyn. **27**, 221–237 (2013).

[32] R. Moura, S. Sherwin, and J. Peiró, "Linear dispersion–diffusion analysis and its application to under-resolved turbulence simulations using discontinuous Galerkin spectral/hp methods," J. Comput. Phys. **298**, 695 – 710 (2015).

[33] M. Franciolini, A. Crivellini, and A. Nigro, "On the efficiency of a matrix-free linearly implicit time integration strategy for high order discontinuous Galerkin solution of incompressible turbulent flows," Comput. Fluids **159**, 276–294 (2017).

[34] Z. Zhang and X. Fuyou, "Spanwise length and mesh resolution effects on simulated flow around a 5:1 rectangular cylinder," J. Wind Eng. Ind. Aerodyn. **202**, 104186 (2020).

[35] J. Jeong, F. Hussain, W. Schoppa, and J. Kim, "Coherent structures near the wall in a turbulent channel flow," J. Fluid Mech. **332**, 185–214 (1997).

[36] A. Cimarelli, A. Leonforte, and D. Angeli, "On the structure of the self-sustaining cycle in separating and reattacching flows," J. Fluid Mech. **857**, 907–936 (2018).

[37] A. Cimarelli, A. Leonforte, E. De Angelis, A. Crivellini, and D. Angeli, "On negative turbulence production phenomena in the shear layer of separating and reattaching flows," Phys. Lett. A **383**, 1019–1026 (2019).

[38] A. Cimarelli, A. Leonforte, E. De Angelis, A. Crivellini, and D. Angeli, "Resolved dynamics and subgrid stresses in separating and reattaching flows," Phys. Fluids **31**, 095101 (2019).

[39] F. Bassi, L. Botti, A. Colombo, A. Crivellini, M. Franciolini, A. Ghidoni, and G. Noventa, "A p-adaptive Matrix-Free Discontinuous Galerkin method for the implicit LES of incompressible transitional flows," Flow

Turbul Combust **105**, 437–470 (2020).

[40] E. Lamballais, J. Silvestrini, and S. Laizet, "Direct numerical simulation of a separation bubble on a rounded finite-width leading edge," Int. J. Heat Fluid Flow **29**, 612–625 (2008).